catalysts

MDPI

Review

Chalcogenides and Chalcogenide-Based Heterostructures as Photocatalysts for Water Splitting

Mohammad Mansoob Khan * and Ashmalina Rahman

Chemical Sciences, Faculty of Science, Universiti Brunei Darussalam, Jalan Tungku Link, Gadong BE1410, Brunei
* Correspondence: mmansoobkhan@yahoo.com or mansoob.khan@ubd.edu.bn

Abstract: Chalcogenides are essential in the conversion of solar energy into hydrogen fuel due to their narrow band gap energy. Hydrogen fuel could resolve future energy crises by substituting carbon fuels owing to zero-emission carbon-free gas and its eco-friendliness. The fabrication of different metal chalcogenide-based photocatalysts with enhanced photocatalytic water splitting have been summarized in this review. Different modifications of these chalcogenides, including coupling with another semiconductor, metal loading, and doping, are fabricated with different synthetic routes that can remarkably improve the photo-exciton separation and have been extensively investigated for photocatalytic hydrogen generation. In this direction, this review is undertaken to provide an overview of the enhanced photocatalytic performance of the binary and ternary chalcogenide heterostructures and their mechanisms for hydrogen production under irradiation of light.

Keywords: semiconductors; chalcogenides; photocatalysts; photocatalysis; water splitting

Citation: Khan, M.M.; Rahman, A. Chalcogenides and Chalcogenide-Based Heterostructures as Photocatalysts for Water Splitting. *Catalysts* **2022**, *12*, 1338. https://doi.org/10.3390/catal12111338

Academic Editors: Gassan Hodaifa, Rafael Borja, Mha Albqmi and Haralampos N. Miras

Received: 19 September 2022
Accepted: 25 October 2022
Published: 1 November 2022

Publisher's Note: MDPI stays neutral with regard to jurisdictional claims in published maps and institutional affiliations.

1. Introduction

Metal oxides and chalcogenides are semiconductors that possess conductivities between those of conductors and insulators and these materials are widely researched semiconductor materials. Due to their stability, resistance to photo-corrosion, non-toxicity, and inexpensive preparation, and the metal oxides such as TiO_2, ZnO, and SnO_2 are commonly applied as photocatalysts [1–4]. Despite these favorable characteristics, a major drawback of using these metal oxides as photocatalysts is their large band gap energies ($\geq$3 eV) [5]. Such wide band gaps only enable them to absorb the ultraviolet portion of the solar spectrum (~4% of the total solar energy), which restricts widespread practical applications [2–4]. Many strategies have been devised to prepare metal oxides with narrower band gaps for improved harvesting of visible light [4,6,7]. However, the scope for band gap tuning by doping and other strategies is limited, and much larger decreases in band gap can be achieved by moving outside the oxide compositional space.

Chalcogenides, compounds comprising one or more electropositive elements and at least one chalcogen ion (S^{2-}, Se^{2-}, or Te^{2-}) [8], are well known for their narrow band gap energies [9,10]. These compounds continue to attract attention due to their numerous desirable properties, including narrow band gap energy, low toxicity, biocompatibility, low cost, and facile synthesis [11,12]. The utilization of chalcogenides and chalcogenide-based semiconductor materials in photocatalytic applications has been reported widely, mainly because of their narrow band gap energies that enable efficient harvesting of visible light [13].

Owing to the devastating impact of conventional fossil fuel use on the environment and the growing demand for energy, an increasing number of countries, companies, and researchers are considering hydrogen (H_2) energy as a potential solution to the pressing environmental and sustainability problems associated with the current global energy system [14]. H_2 is an alternative source of energy because they are clean, non-toxic, eco-friendly, and renewable. Unlike other alternative energy sources, H_2 has the advantage

of producing only water as a by-product upon consumption, which does not cause any pollution or release greenhouse gases [15]. Moreover, the potential clean and green energy source H_2 as a replacement for fossil fuels can be produced in large quantities using simple and low-cost methods [16]. However, H_2 in nature exists in combination with other elements, such as oxygen in water, thus, methods to obtain pure hydrogen should be considered. The production of H_2 employing visible light is one of the most promising approaches for sustainable energy and environmental problems.

Water splitting is a process whereby water molecules are separated into oxygen and hydrogen. The equation for the chemical reaction is as follows:

$$2H_2O \rightarrow 2H_2 + O_2$$

Since pure water in nature does not absorb solar energy readily, a photocatalyst is required for the water-splitting process [17]. The reaction takes place in three steps as shown in Figure 1: step (1) to generate photoexcited electron-hole (e^-/h^+) pairs, the photocatalyst absorbs incoming photons with energies greater than the band gap of the material, step (2) the photogenerated carriers separate and migrate to the catalyst surface, and step (3) surface-adsorbed species (protons, H_2O molecules, and intermediates) are reduced to form hydrogen and oxidized to form oxygen by photogenerated electrons and holes, respectively [18]. According to Maeda and co-workers, the first and second steps depend on the electronic structure and properties of the semiconductor used. In general, high crystallinity promotes water-splitting activity because the density of defects acting as recombination centers is low [19]. In contrast, the third step occurs in the presence of a solid co-catalyst, which is usually a noble metal such as platinum or rhodium, or a metal oxide such as nickel oxide. The loading of the co-catalyst onto the photocatalyst surface provides active sites and lowers the activation energy required for H_2/O_2 gas evolution.

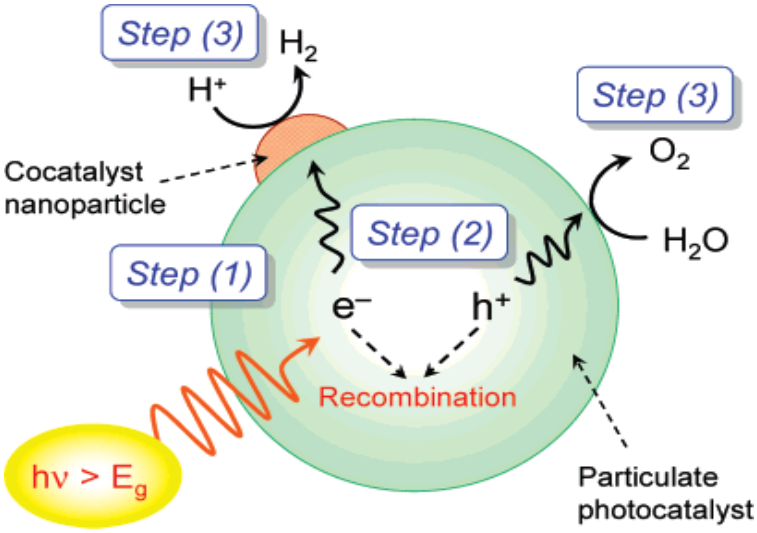

Figure 1. Overall steps involved in the photocatalytic water-splitting process [18].

There are several factors affecting the photocatalytic H_2O splitting as shown in Figure 2. The solar-to-hydrogen conversion efficiency of a material is mainly based on (1) light absorption, (2) e^-/h^+ photogeneration, and (3) separation and migration of e^-/h^+. There are a few principles to keep in mind, including the band gap energy, stability, the use of sacrificial reagents, solution pH, band structure and alignment, effective mass, carrier transport, crystallinity, and surface area of the material used.

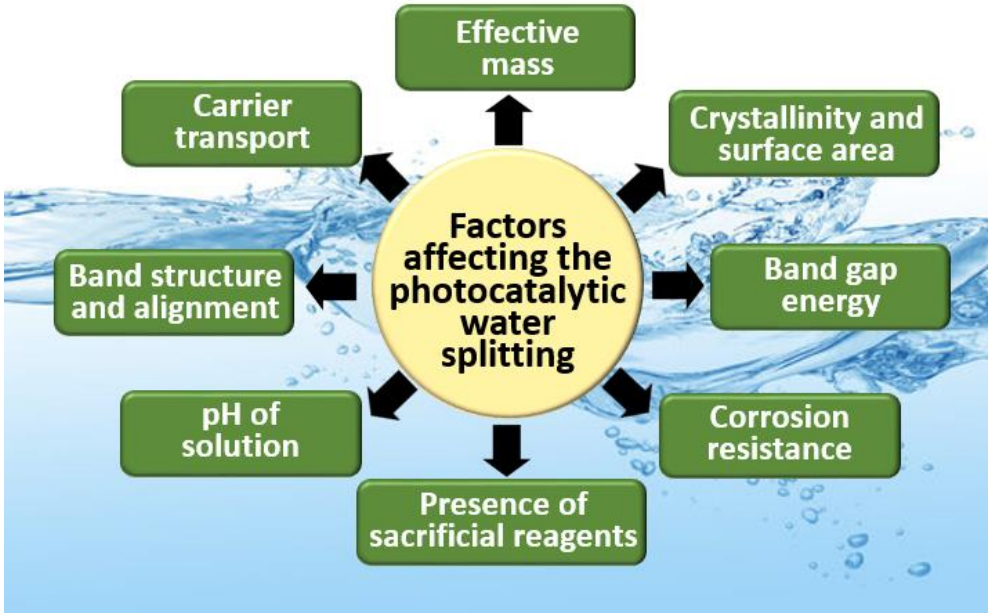

Figure 2. Factors affecting the photocatalytic water-splitting process.

According to Maeda and co-workers, photocatalysts for water splitting under visible-light irradiation must satisfy two requirements; the band gap energy should fall in the range of 1.23 eV (the thermodynamic minimum) to 3.0 eV (the edge of the visible spectrum), and the conduction and valence band edges should align with the H^+/H_2 and H_2O/O_2 redox potentials [19]. In practice, the lower end of the band gap range must be considerably larger than 1.23 eV, perhaps as high as ~2.4 eV, to account for entropic losses in the photocatalyst as well as concentration and kinetic over potential losses. Apart from that, the electron and hole-effective masses are among the key factors for efficient H_2O splitting. For a given mean free time between collisions, a smaller effective mass translates into larger carrier mobility and thus faster charge transport to the semiconductor–liquid interface. In general, the effective mass depends on the crystallographic direction, and therefore certain directions are more favorable for charge transport.

When selecting the material for H_2O splitting, the band edge position is crucial. Their VB should be more positive than the O_2 generation potential, whereas the CB should be more negative than the H_2 generation potential [20]. In addition to possessing a suitable band gap and band edge alignment, photocatalytic materials must have adequate light absorption in the visible region, which accounts for ~43% of the solar energy incident on the earth. The crystallinity and surface-active sites of the selected materials are also important for e^-/h^+ transfer and oxygen evolution reaction (OER)/hydrogen evolution reaction (HER), respectively. Materials with high crystallinity and few defects can reduce the e^-/h^+ recombination. The rate of OER/HER reactions should be larger than backward reactions, which is mostly depending on the number of active sites. Moreover, the material chosen should be stable either in acidic or basic electrolytes.

The present review provides an overview of recent literature on chalcogenides and chalcogenide-based heterostructures, with an emphasis on their synthesis and application for H_2 production by photocatalytic water splitting and the associated mechanisms. The main developments in binary and ternary chalcogenides of different metals including cadmium, copper, gallium, molybdenum, tin, titanium, vanadium, and zinc as well as their heterostructures are summarized. The relevant geometric structures and band structures of these chalcogenides as well as the key optical, electrical, and photocatalytic properties are also highlighted. Finally, the prospects of chalcogenide-based photocatalysts are discussed, and some general conclusions are drawn. The following sections cover the attributes of various chalcogenides and chalcogenide-based heterostructures that have recently been applied to photocatalytic water splitting [19,21].

2. General Synthesis Approaches of Chalcogenides

Although various synthesis methods of chalcogenides have been reported, synthesizing chalcogenides with high stability and to be photocatalytically active simultaneously is very challenging. Appropriate temperature, pressure, metal precursors, source of sulfur, and solvent combinations are important to synthesize these materials. Researchers have developed various synthesis routes for the fabrication of chalcogenides including hydrothermal [22], hot injection [23], solvothermal [24], and sol-gel [25]. Table 1 shows the different synthesis methods of chalcogenides. Gu et al. have synthesized $AgInS_2$ using a low-temperature liquid method and doped it with Mn^{2+} for H_2O splitting [26]. They yielded flower-like $AgInS_2$ spheres with sizes in the range of 200−800 nm. While the particles of Mn-doped $AgInS_2$ (1:100) are spherical with uniform particle sizes of about 300–400 nm. The calculated band gap energies of $AgInS_2$ and Mn-doped $AgInS_2$ (1:100) were found to be 1.63 and 1.52 eV, respectively. The H_2 production rate of $AgInS_2$ is 53 μmol $h^{-1}g^{-1}$. After Mn doping, the H_2 production rate of Mn-doped $AgInS_2$ (1:100) increases slightly, reaching 73 μmol $h^{-1}g^{-1}$. The hydrogen generation of Mn-doped $AgInS_2$ (1:100) was enhanced by loading multi-walled carbon nanotubes, reaching 105 μmol $h^{-1}g^{-1}$, which is ~2 times of $AgInS_2$ and ~1.4 times of Mn-doped $AgInS_2$ (1:100).

Hydrothermal involves a chemical reaction in an aqueous solution at elevated temperature and high pressure. For instance, Kannan et al. have hydrothermally synthesized $Cd_{0.5}Zn_{0.5}S$ using $Cu(NO_3)_2{\cdot}3H_2O$, $Na_2WO_4{\cdot}2H_2O$ and L-Cysteine as the starting materials at different temperatures (120, 140, 160, 180, and 200 °C) for 24 h [22]. Different morphologies, including flake-like and sponge-like examples of $Cd_{0.5}Zn_{0.5}S$, were observed. Moreover, they found that Cu_2WS_4 synthesized at the high temperature of 180 °C and exhibited excellent antibacterial activity against different bacterial strains. This shows that precise control over the reaction conditions, including pressure, time, pH value, concentration, and temperature are necessary for the successful synthesis of chalcogenides. In another study, Yang et al. have successfully fabricated NiS_2 using the hydrothermal method and $Ni(NO_3)_3{\cdot}6H_2O$ as Ni source and thioacetamide as the source of sulfur.

Solvothermal is similar to the hydrothermal method, but it uses a non-aqueous solvent (solvent other than water). For example, Wang et al. have used different $Cd(CH_3COO)_2{\cdot}2H_2O$ and sulfur powder ratios (1:1, 4:5, 2:3, 4:7, 1:2, and 1:3), precursor concentrations (1.5 and 6 mmol), temperatures (100, 140, 180, and 220 °C), and reaction times (4, 24, and 60 h) to yield CdS with different sizes and morphologies using solvothermal method [27]. The authors reported that the morphology, phase composition, and crystallinity of CdS were highly influenced by the precursor ratio, precursor concentration, temperature, and reaction time. The Cd concentration regulated the morphology of CdS morphology due to its effect on the formation of shape-determinant CdS nuclei. Nanorods, multipods, and triangular-like shape CdS nanocrystals were obtained with 1.5, 3, and 6 mmol of Cd, respectively. The arm diameter in CdS multipods increases from 10 to 60 nm with the sulfur concentration increasing when the cadmium concentration is maintained at 3 mmol.

Table 1. Different preparation methods of chalcogenides.

Synthesized Materials	Synthesis Method	Metal Precursor Used	Source of Sulfur	Solvent Used	Ref.
$AgInS_2$	Low-temperature liquid method	$AgNO_3$ $In(NO_3)_3{\cdot}xH_2O$	Thioglycollic acid Thioacetamide	Water	[26]
$AgInS_2$	Microwave	$AgNO_3$ $In(NO_3)_3{\cdot}4.5H_2O$	Sulfur powder	Glycerol, Oleic acid, Oleylamine, 1-dodecanethiol and 1-octadecene	[28]
$Cd_{0.5}Zn_{0.5}S$	Hydrothermal	$Cd(CH_3COO)_2{\cdot}2H_2O$ $Zn(CH_3COO)_2{\cdot}2H_2O$	$Na_2S{\cdot}9H_2O$	Water	[29]

Table 1. *Cont.*

Synthesized Materials	Synthesis Method	Metal Precursor Used	Source of Sulfur	Solvent Used	Ref.
CdS	Solvothermal	$Cd(CH_3COO)_2 \cdot 2H_2O$	Sulfur powder	Dodecylamine	[27]
Cu_2WS_4	Hydrothermal	$Cu(NO_3)_2 \cdot 3H_2O$ $Na_2WO_4 \, 2H_2O$	L-Cysteine	Water	[22]
Cu_2WSe_4	Hot injection	$CuCl_2 \cdot 2H_2O$ WCl_4	Se powder	Oleylamine	[23]
Cu_2ZnSnS_4	Hot injection	$Cu(acac)_2$ $Zn(OAc)_2 \cdot 2H_2O$ $Sn(OAc)_4$	1-dodecylthiol and tert-dodecylthiol	1-octadecene	[30]
$CuCdS_2$	Solvothermal	Copper nitrate Cadmium acetate	Sodium thiosulphate pentahydrate	Ethylene glycol	[24]
CuS	Hydrothermal	Copper acetate dihydrate	Thiourea	Water	[31]
MoS_2	One-pot liquid-phase reaction	$(NH_4)_6Mo_7O_{24}$	Na_2S	Water	[32]
NiS_2	Hydrothermal	$Ni(NO_3)_3 \cdot 6H_2O$	Thioacetamide	Water	[33]
VS_2	Single-step chemical vapor deposition	VCl_3	Sulphur powder	-	[34]
$Zn_{0.5}Cd_{0.5}S$	Combustion method	$Zn(NO_3)_2 \cdot 4H_2O$, $Cd(NO_3)_2 \cdot 6H_2O$	Thioacetamide	Water	[35]
ZnS	Co-precipitation	$Zn(NO_3)_2$	Na_2S	Water	[36]

Microwave-assisted synthesis is reported to be a clean, fast, and convenient synthetic route of chalcogenides. It works by applying microwave irradiation to chemical reactions which is based on efficient heating [5]. For example, Hu et al. have successfully synthesized $AgInS_2$ with tunable composition and optical properties using microwave-assisted synthesis [28]. In another study, the co-precipitation reaction between Na_2S solution and $Zn(NO_3)_2$ at room temperature produced ZnS [36]. The combustion method carried out by Tang et al. to produce $Zn_{0.5}Cd_{0.5}S$ using $Zn(NO_3)_2 \cdot 4H_2O$, $Cd(NO_3)_2 \cdot 6H_2O$ and thioacetamide [35]. Using water as the solvent, they heated the starting materials on the heating jacket until the gel-like precursor was formed, then the precursor was transferred into a Muffle furnace and heated at 300 °C for 15 min which resulted in the formation of yellow $Zn_{0.5}Cd_{0.5}S$ solid. Chemical vapor deposition (CVD) is a technique that uses thermally induced chemical reactions at the surface of a heated substrate. For example, Gopalakrishnan et al. have deposited VS_2 on the surface of vertically aligned Si nanowires using the CVD method [34]. In the typical synthesis, they used VCl_3 and sulfur powder as the precursors of V and S, respectively.

Based on the findings, it can be observed that the properties of chalcogenides can be tuned by controlling the reaction parameters during synthesis. Therefore, the optimization of these parameters is of crucial importance to fabricate the desired properties of chalcogenides with enhanced H_2O splitting ability.

3. Binary Chalcogenides and Their Photocatalytic Water-Splitting Activities

H_2 is a clean fuel, and its usage can address many of the issues caused by using fossil fuels. It has several uses, as shown in Figure 3; it is widely used as a feedstock in the chemical industry to produce ammonia, methanol, and various fuels like diesel, gasoline, etc. It is also used as a transport fuel. It has several other applications in the production of metals and agricultural industries. A cost-effective and long-lasting chalcogenide-based photocatalysts can make the H_2 generating process more economical and suitable. The use of binary chalcogenides and their modifications (compounds consisting of only one chalcogen and one electropositive atom [10]) for photocatalytic water splitting will be discussed in the following subsections.

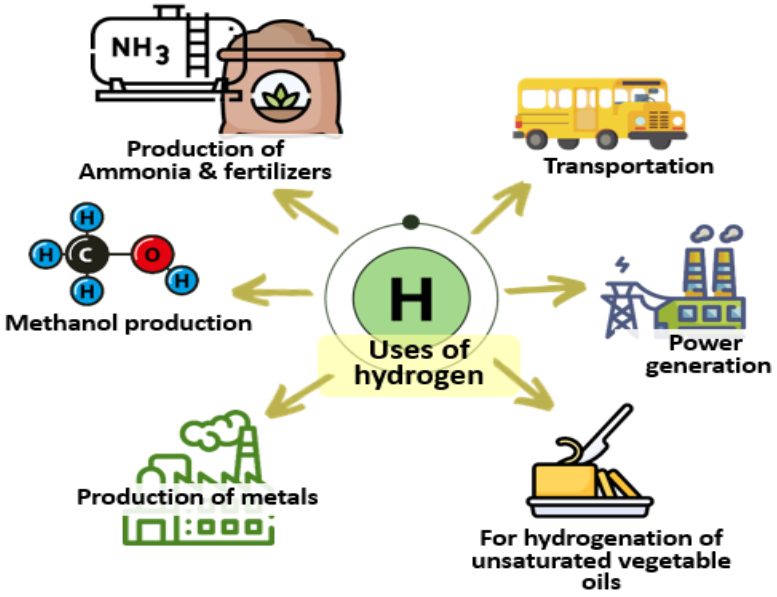

Figure 3. Several applications of H_2.

3.1. Cd-Based Chalcogenides

CdS and CdSe have both been used extensively in the fields of photocatalysis and photovoltaics, particularly in photoelectrochemical cells. Despite having a favorable bandgap for water splitting (~2.42 eV) [37,38] CdS is unstable in an aqueous solution under light irradiation due to photocorrosion. Therefore, in order to improve its photostability and photocatalytic activity, many studies have focused on synthesizing different morphologies of CdS together with the addition of co-catalysts and sacrificial agents [38]. Some of the different morphologies of CdS nanostructures that have been studied include hollow spheres [27], quasi-nanospheres [39], nanowires [39], and nanotubes [39], all of which can be synthesized by hydrothermal methods. Among these, CdS nanospheres were found to exhibit the highest H_2 evolution rate during photocatalytic testing in the presence of Na_2SO_3 and Na_2S hole scavengers.

In a recent study, one-dimensional CdS nanotubes displayed a remarkably high valence band edge compared with bulk CdS due to quantum confinement effects, and it was found that the photocatalytic efficiency of CdS nanotubes is higher than that of bulk CdS. Furthermore, the stabilized valence band, tubular structure, and strong p-d orbital hybridization led to a significant enhancement in photostability, making applications in aqueous solutions feasible [40].

In addition to the aforementioned studies focused on enhancing CdS through the preparation of different morphologies and sizes, another strategy to impart anti-photocorrosion properties to CdS is surface-modification with non-noble co-catalysts such as Ni, Ni_2P, and CuS-Ni_xP [41–43] as well as noble metals such as Pt and Au [44,45].

Another strategy to improve the photostability of CdS in an aqueous solution is to coat it with a thin layer of ZnO. Tso and co-workers have synthesized composite nanowires comprising CdS cores covered with thin ZnO shells, yielding CdS/ZnO core–shell nanowires [46]. These heterostructures provided improved stability compared with bare CdS nanowires and also led to reduced electron-hole recombination, causing an increase in H_2 evolution activity of over two orders of magnitude as shown in Figure 4. Investigations also revealed that nanowires with 10–30 nm-thick shells absorbed more incident light than nanowires with thinner ZnO shells and had a lower probability of electron-hole recombination, the combination of which led to higher H_2 evolution activity.

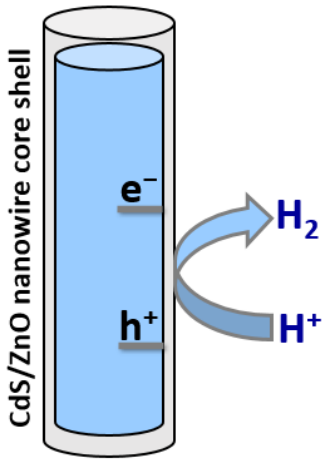

Figure 4. Schematic diagram of photocatalytic H_2 production using CdS/ZnO core–shell nanowire.

Several recent studies have examined photogenerated electron-hole pair separation in CdS/CuS nanocomposites [46]. Pan and co-workers found a high H_2 evolution rate of 561.7 μmol h^{-1} during photocatalytic water splitting using a CdS/CuS nanocomposite [47]. In another work, a CdS/CuS nanostructured heterojunction was synthesized [48]. The prepared material was applied as a water-splitting photocatalyst and showed that the nanocomposites exhibit an enhanced rate of photocatalytic H_2 evolution under visible-light irradiation. It can be concluded that CuS as a non-noble catalyst can improve the stability of CdS for photocatalytic H_2 production in an aqueous solution. The enhancement in stability found in the CdS/CuS system can be explained by the transfer of holes from CdS to CuS, which inhibits the photocorrosion of CdS (Figure 5) [49].

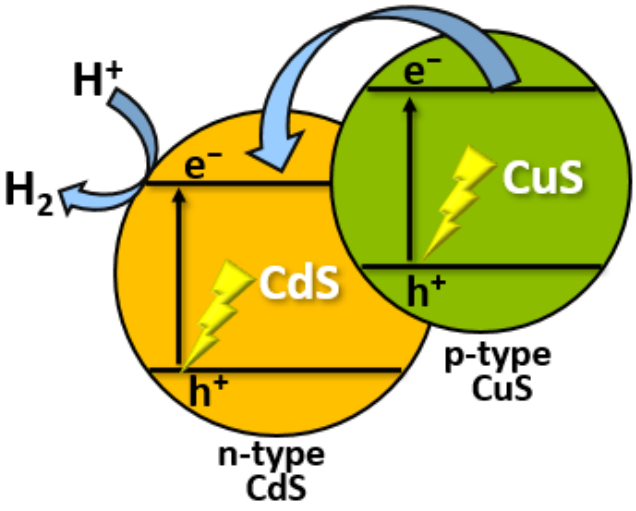

Figure 5. Mechanism of photocatalytic H_2 evolution using CdS/CuS nanocomposite.

Several authors have studied the factors affecting the performance of nanocrystalline CdSe quantum dots (QD) in photocatalytic water-splitting applications. Osterloh and co-workers showed a clear relationship between the extent of quantum size confinement and the photocatalytic water-splitting activity of suspended CdSe QDs. They found that the rate of H_2 evolution increased with QD size in nm as follows: 2.20 > 2.00 > 2.48 > 1.75 > 2.90 > 2.61 > 2.75 > 3.05 > 3.49 > 4.03 > 4.81. These results confirm that photocatalytic activity can be controlled by the extent of quantum confinement (Figure 6) [50].

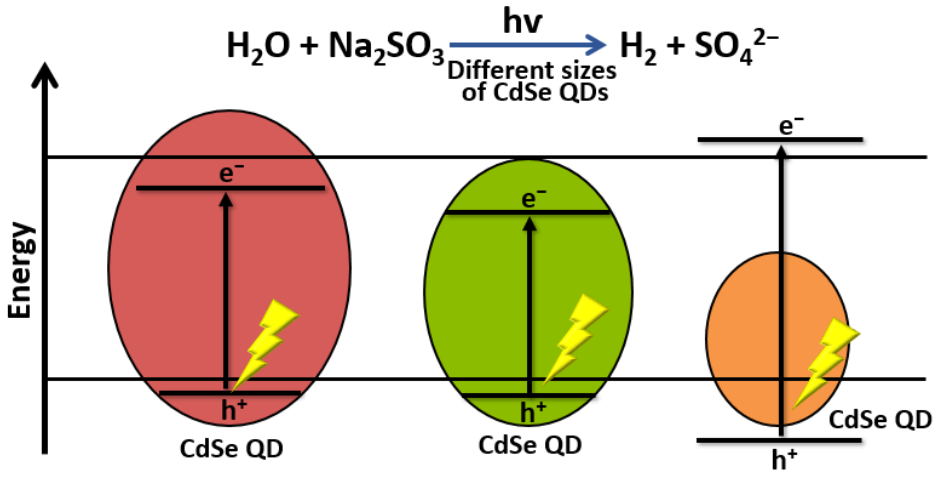

Figure 6. Schematic illustration of the effect of CdSe QD size in photocatalytic H_2 production.

Covalent organic frameworks (COFs) have drawn research interest owing to their stability, porous structure, large surface area, and tunable band structure [51]. It is an organic polymer arranged periodically with high crystallinity and high porosity, that is built from the integration of selected organic blocks via covalent bond linkage [52]. For instance, You et al. have synthesized COFs-p-phenylenediamine@CdS (COFs-Ph@CdS) using the hydrothermal method [53]. The authors reported that of the H_2 generation of bare CdS, COFs-Ph@CdS-x (x = 1, 2, 3, 4) photocatalysts were 16.4, 139.1,17.5, 37.0, and 15.2 µmol, respectively. The photocatalytic H_2 production activity of solid COFs-Ph@CdS-1 exhibited 29 and eight times higher compared to those of pristine COFs and CdS, respectively. The enhanced activity may be attributed to a stable coordination bond between Cd^{2+} ions and N atoms in COFs-Ph@CdS was formed, which served as a migrated channel for photo-generated carriers and their unique hollow structure that enables the production of more photo-generated electrons and holes and absorb light more efficiently.

High rates of photocatalytic H_2 production were demonstrated by Das and co-workers using a surface ligand that binds strongly to CdSe QDs via tridentate coordination [54]. These authors also reported the effects of surface stabilizing and solubilizing agent dynamics. In more recent work, the influence of ligand exchange on the photocatalytic activity of CdSe QDs in solar water-splitting cells was studied [55]. It was found that CdSe QDs bearing shorter ligands showed better photocatalytic activity when compared to pristine CdSe QDs in a photoelectrochemical cell. These results should assist with the design and optimization of photochemical energy conversion systems employing nanocrystalline CdSe QD photocatalysts.

In another study, Zhou et al. have successfully prepared peanut-chocolate-ball-like CdS/Cd for H_2 evolution [56]. They reported that CdS/Cd exhibited a high photocatalytic H_2 production of 95.40 lmol h^{-1} which is about 32.3 times higher than bare CdS and displays exceptional photocatalytic stability over 205 h in comparison to CdS-based photocatalyst reported in previous studies. In recent studies, Li et al. 2% NiS/CdS present a high H_2 evolution rate of 18.9 mmol $g^{-1}h^{-1}$ in comparison to pristine CdS [57]. The improved activity may be attributed to the presence of an interface between NiS and CdS that efficiently promote the charge separation and NiS nanoparticles serve as highly active H_2 evolution sites.

3.2. Cu-Based Chalcogenides

Visible-light-active CuS/Au nanostructures were obtained by decorating CuS particles with Au nanoparticles, which were prepared by reducing $HAuCl_4$ on the CuS surface [58]. The as-synthesized nanostructures displayed excellent catalytic performance in electrochemical H_2 evolution tests, with good durability under acidic conditions. It was found that the CuS/Au nanostructured catalyst could produce a current density of 10 mA/cm^2

upon the application of only 0.179 V versus the reversible hydrogen electrode (RHE). The CuS/Au catalyst also proved to be an efficient photocatalyst for the degradation of organic pollutants under visible-light irradiation.

The coupling of CuS with metal oxide has been shown to enhance its photocatalytic activities. For instance, Chandra and co-workers have synthesized CuS/TiO_2 heterostructures with varying TiO_2 contents using a simple hydrothermal method for the photocatalytic evolution of H_2 [59]. The highest rate of visible-light photocatalytic H_2 production was 1262 μmol h^{-1} g^{-1}, which is around 9.7 and 9.3 times faster in comparison to pristine TiO_2 nanospindles or CuS nanoflakes, respectively. The enhanced rate of H_2 evolution is attributable to increased light harvesting and more efficient charge separation when an optimum amount of CuS is deposited on TiO_2. Growing CuS nanoflakes on TiO_2 nanoparticles to form a CuS/TiO_2 heterostructure facilitates charge carrier separation at the heterostructure interface and thus enhances photocatalytic performance.

In another study, Dubale et al. fabricated nanocomposites comprising CuS and Cu_2O/CuO heterostructures with and without decoration by Pt nanoparticles using an in-situ growth method [60]. Cu_2O/CuO was prepared by straightforward anodization of Cu film, and a sputtering technique was used to deposit Pt nanoparticles onto the prepared Cu_2O/CuO/CuS photocathodes. The prepared heterostructures were found to be very promising and highly stable photocathodes for H_2 evolution under visible-light irradiation, with optimized Cu_2O/CuO/CuS photocathodes reaching photocurrent densities of up to 5.4 mA cm^2, some 2.5 times higher than that achieved by bare Cu_2O/CuO. Upon decorating the Cu_2O/CuO with both CuS and Pt, a further increase in photocurrent density to 5.7 mA/cm^2 was achieved due to the suppression of the charge carrier recombination.

Metal loading on the surface of Cu-based chalcogenides has been reported to improve the photocatalytic evolution of H_2. For instance, Ma and co-workers have reported that hydrothermally synthesized Au/CuSe/Pt nanoplates showed strong dual-plasmonic resonance and have been employed for photocatalytic H_2 generation under irradiation of visible and near-infrared [61]. The as-prepared Au/CuSe/Pt nanoplates exhibited outstanding H_2 generation activities of around 7.8 and 9.7 times those of Au/CuSe and Pt/CuSe composites, respectively. In the Au/CuSe/Pt system, light harvesting is enhanced by the plasmonic units (CuSe and Au), while Pt is mainly present as a co-catalyst promoting the H_2 evolution reaction as shown in Figure 7.

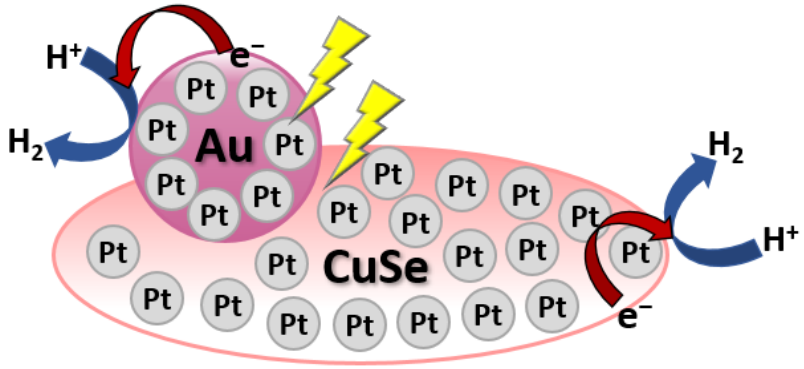

Figure 7. Schematic diagram of Au/CuSe/Pt ultrathin nanoplate hybrid for H_2 evolution under visible and near-infrared irradiation.

In a study conducted by Liang et al. CuS was deposited on the surface of CdS nanorods using the cation exchange method for generation of H_2 under the irradiation of light [62].

In a study by Hou et al., CuS has been used as a co-sensitizer along with CdS to improve photocatalytic H_2 production [63]. They decorated CdS–CuS on TiO_2 nanotube arrays using the hydrothermal method. The as-prepared material exhibited remarkably high photocatalytic H_2 evolution ability, and the photocatalytic H_2 production rate was about 62.02 μmol $cm^{-2}h^{-1}$. In a different study, Mandari and co-workers synthesized a stable CuS/Ag_2O/g-C_3N_4 material using hydrothermal and precipitation methods [31].

The as-synthesized material displayed a remarkable photocatalytic H_2 production of 1752 μmol $h^{-1}g^{-1}$ which is considerably superior to those of the pristine CuS and g-C_3N_4. The enhanced H_2 production activity may be ascribed to the formation of heterojunctions which resulted in the increase in visible light harvested and suppressed the photogenerated charge carrier recombination.

3.3. Ga-Based Chalcogenides

Monolayers of GaS and GaSe have been studied as photocatalysts by several authors but their performance is limited by low optical absorption and inefficient electron-hole pair separation [64,65]. One strategy to overcome these limitations is the construction of van der Waals (vdW) heterostructures by pairing GaX (GaX, X = S, Se) with arsenene (two-dimensional arsenic), as demonstrated by Peng and co-workers using first-principle calculations [66]. Such GaX/As heterostructures possess band gaps and band alignment that satisfy the requirements for photocatalytic water splitting. In contrast to pristine GaX monolayers, the type of band gap in $Se_{0.5}GaS_{0.5}$/As and $S_{0.5}GaSe_{0.5}$/As changes favorably from indirect to direct as the interlayer distance is varied. Furthermore, these heterostructures exhibit transport anisotropy with high electron mobilities of up to ~2000 cm^2 V^{-1} s^{-1}, which facilitates photogenerated electron-hole pair separation and migration. All of the GaX/As heterostructures studied also show enhanced visible-light absorption beyond that of pristine GaX monolayers. It seems likely that the exceptional properties of GaX/As heterostructures will render them competitive with existing photocatalysts for solar-driven water splitting [66].

3.4. Mo-Based Chalcogenides

Molybdenum disulfide (MoS_2) is a two-dimensional (2D) material, and it tends to exhibit more remarkable photocatalytic properties than its bulk counterparts [67,68]. Li and co-workers have investigated the photocatalytic properties of pristine MoS_2 nanosheets and Ag-modified MoS_2 nanosheets. They found that the rate of photocatalytic H_2 production by Ag-modified MoS_2 nanosheets could reach 2695 μmol h^{-1} g^{-1}. They also found that Ag-doped MoS_2 nanosheets exhibit superior stability and higher H_2 evolution efficiency compared with pristine MoS_2 nanosheets, which is mainly due to increased visible-light absorption with increasing Ag content (Figure 8) [69].

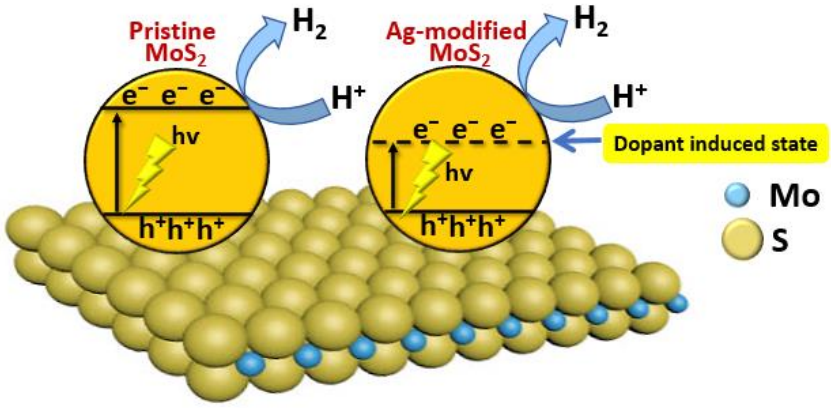

Figure 8. The mechanism of photocatalytic H_2 production using Ag-modified MoS_2 nanosheets.

Photocorrosion-resistant material, $MoS_2/Zn_{0.5}Cd_{0.5}S$/g-C_3N_4, has been successfully synthesized by Tang et al. to produce H_2 under irradiation of visible light [35]. The authors reported that the as-prepared materials exhibited a maximum H_2 production rate of 4914 μmol $g^{-1}h^{-1}$ in Na_2S-Na_2SO_3 solutions which served as the sacrificial agent. The high evolution rate of H_2 was owing to the improved charge separation between the interfaces.

In another study, Yuan et al. designed 2D-2D MoS_2@Cu-$ZnIn_2S_4$ using the solvothermal method for photocatalytic production of H_2 [70]. The highest H_2 evolution rate of 5463 μmol $g^{-1}h^{-1}$ was observed for 6% MoS_2@Cu-$ZnIn_2S_4$ under irradiation of visible light which is 72 times higher than that of pristine Cu-$ZnIn_2S_4$. The excellent activity may be ascribed to the high visible light absorption property and abundant active sites for the H_2 evolution reaction to take place. Moreover, the production rate of H_2 remain unchanged after three cycles which suggested the high durability of the synthesized MoS_2@Cu-$ZnIn_2S_4$ for photocatalytic H_2 production.

An enhanced photocatalytic H_2 evolution was performed by Yin and co-workers with the maximum evolution rate of 872.3 mol h^{-1} using MoS_2/C composites sensitized with Erythrosin B [32]. The enhanced performance was attributed to the efficient photogenerated charge transfer and separation between Erythrosin B and MoS_2 or C as well as the presence of more active sites for H_2 evolution. The photocatalytic evolution of H_2 could also be achieved through photoelectrochemical catalytic activities. For instance, Hassan and co-workers have reported the optimized MoS_2/GaN_2 exhibited significantly higher photoelectrochemical performance in comparison to the bare materials under the same visible conditions [71]. The as-prepared photoanode achieved efficient light harvesting with a photocurrent density of 5.2 mA cm^{-2} which is 2.6 times higher than bare GaN. Moreover, MoS_2/GaN_2 exhibited enhanced applied-bias-photon-to-current conversion efficiency of 0.91%, while the reference GaN yielded an efficiency of 0.32%. The authors reported that the decrease in charge transfer resistance between the electrolyte and semiconductor interface and the improved separation charge carriers in the MoS_2/GaN heterostructures were all attributed to significant improvements in photocurrent density and efficiency.

MoS_2-based nanomaterials have been found to be an efficient visible light-responsive material for H_2 production. Based on the reported work, revealed that the surface modification of the MoS_2 could lead to an improved photocatalytic activity owing to the effective charge transfer and separation of photo-generated e^-/h^+ pairs.

New strategies have been developed to use $MoSe_2$-based nanosheets as photocatalysts for the H_2 evolution reaction. Zhao and co-workers achieved an enhancement in the photocatalytic activity of $MoSe_2$ by surface modification and doping with Ni and Co [72]. Their study found that $Ni_{0.15}Mo_{0.85}Se_2$ nanosheets exhibited the highest photocatalytic activity in both alkaline and acidic media. These results provide an attractive alternative to Pt-based catalysts.

3.5. Sn-Based Chalcogenides

Recently, it has been discovered that monolayers of the Sn-based mono- and dichalcogenides SnX and SnX_2 (X = S or Se) are promising candidates for photocatalytic water splitting. These materials exhibit very good visible light absorption, low exciton binding energies, and high carrier mobility. However, in their pure and strain-free state, the valence band edges of Sn-monochalcogenide monolayers are predicted to be too high in energy for effective water oxidation. This issue can potentially be overcome by crystal engineering to induce a moderate tensile strain, which is predicted to lower the valence band edge to a level suitable for water oxidation [21]. Li and co-workers reported that monolayers of both SnX and SnX_2 are expected to exhibit good optical absorption in the visible region of the solar spectrum, and the predicted sequence of visible light absorption strength is as follows: SnSe > $SnSe_2$ > SnS > SnS_2. Moreover, SnX and SnX_2 monolayers also have excellent carrier mobility, which results in the fast migration of photogenerated carriers to the surface. Hence, the possibility of rapid redox reactions on the surface of the photocatalyst.

In another study, Lei et al. successfully prepared SnS/g-C_3N_4 nanosheets using a facile ultrasonic and microwave heating approach, which formed intimate interfacial contact and a suitable energy band structure [73]. The optimized sample displayed enhanced photocatalytic H_2 evolution from H_2O with the aid of Pt as a co-catalyst in comparison to pure g-C_3N_4. The stability of the photocatalysts was significantly improved after being loaded with MoO_3 particles due to the formation of a Z-scheme heterojunction. Among

all as-prepared samples, the 10% SnS/g-C_3N_4 exhibits the highest photocatalytic rate of 818.93 mmol $h^{-1}g^{-1}$ under AM1.5G irradiation, 2.90 times to pure g-C_3N_4, due to the matched energy band structure between g-C_3N_4 and SnS, which improves the separation efficiency of photo-generated carriers and hinders the recombination of hole-electron pairs. Additionally, SnS nanosheets have improved the light absorption efficiency of the prepared material and generated more catalytic active sites as well as shortening the carriers' transport path as well.

Liu and co-workers have synthesized flower-like nanostructure SnS_2 with generated sulfur vacancies using a new simple strategy of ion exchange [74]. The morphology of the flower-like structure provides shorter carrier diffusion lengths and more surface-active sites. While, the presence of S vacancies helps introduce defect levels in SnS_2, which leads to a reduction in work function, eventually improving carrier density and separation efficiency. The well-engineered sample 5%Cu/SnS_{2-x} shows the highest photocatalytic activity with an H_2 yield of 1.37 mmol h^{-1}, which is about six times higher than that of pure SnS_2.

$SnS_2/ZnIn_2S_4$ composites were successfully fabricated by decorating SnS_2 nanosheets with $ZnIn_2S_4$ microspheres [75]. Geng and co-workers reported that the $SnS_2/ZnIn_2S_4$ composites showed superior photocatalytic properties for H_2 generation in comparison to pristine $ZnIn_2S_4$. Furthermore, a notable impact was observed on the photocatalytic activity of $ZnIn_2S_4$ when varying the mass ratio of SnS_2. The 2.5% $SnS_2/ZnIn_2S_4$ in particular exhibited the highest photocatalytic H_2 generation rate of 769 μmol $g^{-1}h^{-1}$, which was about 10.5 times the photocatalytic activity of pristine $ZnIn_2S_4$. The enhanced photocatalytic activity may be due to the formation of $SnS_2/ZnIn_2S_4$ heterojunction, which enabled highly active charge separation and transfers on the interface of SnS_2 and $ZnIn_2S_4$.

Li and co-workers have synthesized SnO_2/SnS_2 with excellent photocatalytic H_2 evolution performance under simulated light irradiation [76]. The material exhibited a high H_2 production rate of 50 μmol h^{-1} which is 4.2 times higher than that of pure SnO_2 under the same condition. A different study by Mangiri et al. has successfully synthesized a stable CdS/MoS_2-SnS_2 for water splitting via the solvothermal method [77]. The as-prepared CdS/MoS_2-SnS_2 (6 wt%) exhibited the highest H_2 production rate of 185.36 mmol $h^{-1}g^{-1}$ which is much higher than pristine CdS (2.5 mmol $h^{-1}g^{-1}$) and 6 wt% of MoS_2-loaded CdS nanorods (123 mmol $h^{-1}g^{-1}$). The effective photocatalytic performance of MoS_2-SnS_2-loaded CdS may be ascribed to the ability of the material to harvest light effectively, better separation of e^-/h^+ pairs, formation of trapping sites, high active catalytic zones, migration of charge carriers towards the surface of a semiconductor, and suitable energy levels.

3.6. Ti-Based Chalcogenides

The tri-chalcogenide TiS_3 was found to be an effective photoanode for use in photoelectrochemical cells. Photocatalytic H_2 evolution rates of up to 1.80 ± 0.05 μmol min^{-1} were obtained, corresponding to a photoconversion efficiency of ~7% [78]. Furthermore, the ternary compounds $Ti_xNb_{1-x}S_3$ (Nb-rich) and $Nb_xTi_{1-x}S_3$ (Ti-rich) were tested as photoanodes and compared with the corresponding binary trisulfides. The binary compounds were polycrystalline with a nanoribbon morphology and adopted the monoclinic TiS_3 (P21/m) and triclinic NbS_3 (P2) crystal structures, respectively. H_2 generation experiments revealed that the Ti-rich phase was a superior photocatalyst compared with the Nb-rich phase, exhibiting H_2 production rates of up to 2.2 ± 0.1 mol/min cm^2 [79]. Ti-based chalcogenides are not widely explored for their photocatalytic H_2 production activity. Therefore, further studies and optimizations are required.

3.7. V-Based Chalcogenides

Certain transition metals located on the first row of the periodic table can participate in the formation of tetra-chalcogenides thanks to their ability to adopt +4 oxidation states (Figure 9). Among these metals is vanadium, which can form the binary tetra-chalcogenide VS_4. Nanocomposites comprising VS_4 and graphene were evaluated for solar-driven water splitting by Guo and co-workers. Excellent performance was obtained due to the formation

of C–S bonds with a π-conjugated structure, which assists with transferring electrons from the S 2p orbital to graphene [80]. The ternary tetra-chalcogenides $Cu_3Nb_{1-x}V_xS_4$ and $Cu_3Ta_{1-x}V_xS_4$, which exist as solid solutions and adopt the sulvanite structure, were successfully synthesized in a solid-state reaction by Ikeda and co-workers [81]. The band gaps of the synthesized materials were estimated to fall in the range of 1.6–1.7 eV, and the band structure of the $Cu_3M_{1-x}V_xS_4$ system varies with composition. It was found that for most compositions of solid solution, superior photocatalytic activity was achieved compared with the ternary Cu_3MS_4 (M = V, Nb, Ta) compounds [81].

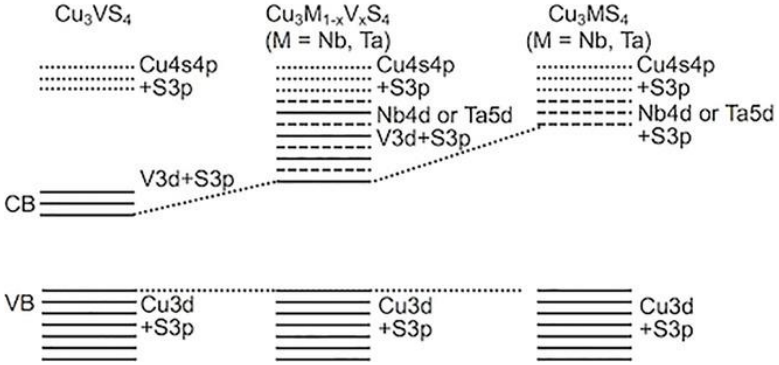

Figure 9. Proposed band structures for $Cu_3M_{1-x}V_xS_4$ (M = Nb and Ta) solid solutions.

Li et al. synthesized the $VS_2@C_3N_4$ heterojunction with S vacancies via the in situ supramolecular self-assembly method [82]. The as-synthesized material shows a remarkable synergistic H_2 production rate (9628 μmol $g^{-1}h^{-1}$) and wastewater degradation efficiency as well as stability, which is 16.0 times that of pristine C_3N_4. Based on the theoretical calculations and experiment findings, it shows that S vacancies have resulted in the formation of compact heterostructure and the reduction in the work function, which promotes interfacial carriers' transfer and surface properties. The core–shell structure improves the stability of S vacancies.

In another study, Gopalakrishnan et al. synthesized a core–shell heterostructures photocathode consisting of VS_2 deposited on a silicon nanowire surface via single-step chemical vapor deposition for H_2 evolution under solar irradiation [34]. The core–shell nanowire heterostructure photocathode displayed an outstanding solar-assisted water reduction performance at pH∼7 over a pristine photocathode. The as-prepared material produces about 23 μmol cm^{-2} h^{-1} (at 0 V vs. RHE) of H_2 gas. Recently, Zhong et al. have doped Ni_3S_2 with nitrogen and coupled it with VS_2 using the hydrothermal method [83]. Based on their results, Ni_3S_2/VS_2 without nitrogen doping exhibited improved oxygen evolution reaction (OER) performance with an extremely low overpotential of 227 mV at 10 mA/cm^2 which may be attributed to the presence of high number of active sites and excellent interfaces. Moreover, Ni_3S_2/VS_2 with nitrogen doping shows high electrocatalytic hydrogen evolution reaction (HER) performance with a low HER overpotential (151 mV at 10 mA/cm^2) and this is due to the presence of nitrogen doping that significantly improves the conductivity and increases the number of catalytic active sites.

3.8. Zn-Based Chalcogenides

Kurnia and co-workers have investigated the performance of ZnS thin films during photoelectrochemical H_2 generation [84]. They found that ZnS is an inexpensive photocatalyst that exhibits activity under visible-light irradiation without the addition of a co-catalyst. The ZnS thin films were estimated to have band gaps of ~2.4 eV, and photocurrent densities exceeding 1.5 mA/cm^2 were achieved under visible-light irradiation ($\lambda \geq 435$ nm). These photocurrents are remarkably high for H_2 generation by undoped ZnS under visible-light irradiation.

A modification of ZnO nanosheets, using a thin layer of ZnS, was developed to enhance visible light absorption, leading to improved photoelectrochemical activity in water-

splitting experiments [85,86]. Sánchez-Tovar and co-workers have prepared ZnO/ZnS heterostructures using anodization of Zn in glycerol/water/NH_4F electrolytes under controlled hydrodynamic conditions in the presence of various concentrations of Na_2S [85]. In another work, Zhang et al. synthesized ZnS/ZnO/ZnS sandwich nanosheets with an effective band gap of ~2.72 eV using thermal evaporation, and these materials resulted in potent visible-light photocatalytic activity [86]. These works show that coating ZnO with an ultrathin surface layer of ZnS is an interesting approach for enhancing its water-splitting activity under solar irradiation.

Arai and co-workers have synthesized hollow Cu-doped ZnS particles as visible-light photocatalysts for the decomposition of hydrogen sulfide under solar irradiation to generate H_2. The Cu-doped ZnS particles were synthesized starting from a ZnO precursor that was co-precipitated on Cu by exploiting the difference in reduction potential between Zn and Cu. The visible-light photoactivity of Cu-doped ZnS was six- and 130-times higher than the Cu-free "ZnS-shell" and pristine ZnS particles prepared using co-precipitation, respectively. A comparative study found that the "Cu-ZnS-shell" particles were highly active under visible-light irradiation ($\lambda > 440$ nm), and the rate of H_2 evolution was optimized with a Cu (2 wt%)/ZnS photocatalyst [36]. In another recent study, Cu/ZnS microspheres were prepared using a template-free microwave irradiation method for H_2 generation from an aqueous Na_2S solution under visible-light irradiation. The optimized H_2 evolution rate of 973.1 μmol h^{-1} g^{-1} was obtained for 2.0 mol% Cu-doped ZnS [87].

4. Ternary Chalcogenide Heterostructures for Water Splitting

Recently, ternary mixed-metal chalcogenides have shown excellent photocatalytic H_2 production activities, as shown in Table 2. For instance, $Zn_xIn_2S_{3+x}$ (x = 1–5) has attracted the attention of researchers as a new member of the semiconductor family. These compounds possess unique electronic structures, tunable optical properties, and, for certain compositions, band gaps suitable for visible-light absorption and energy bands that straddle the water redox potentials, making them ideal for use in photocatalysis and energy conversion reactions [88]. Wu and co-workers have successfully synthesized $Zn_xIn_2S_{3+x}$ with *x* ranging from 1 to 5 [88]. $Zn_xIn_2S_{3+x}$ samples display strong absorption of visible light due to excitation of the fundamental band gap transition, and the absorption edges of the samples move to a shorter wavelength as x is increased from 1 to 5 due to the widening of the band gap. $Zn_xIn_2S_{3+x}$ samples have band gap energies ranging from 2.65 eV to 2.84 eV, depending on chemical composition. $ZnIn_2S_4$ exhibited the lowest electron-hole recombination rate among all the compositions studied. One of the contributing factors leading to this finding is the presence of fewer composition faults in the $ZnIn_2S_4$ structure compared with the other samples. The existence of composition faults results in additional energy barriers to be overcome by charge carriers during transit to the particle surface, which leads to increased recombination and lower photocatalytic reaction rate. Based on the photoelectrochemical experiments conducted, it was found that $ZnIn_2S_4$ can generate more photocurrent than the other compositions. Electrochemical impedance spectroscopy results also suggest that $ZnIn_2S_4$ has the lowest resistance to interfacial electron transfer among the compositions studied, suggesting that $ZnIn_2S_4$ is the most efficient at interfacial charge transfer and consistent with the photocurrent trend. $ZnIn_2S_4$ shows the highest photocatalytic activity, followed by $Zn_2In_2S_5$, $Zn_3In_2S_6$, $Zn_4In_2S_{7,}$ and, lastly, $Zn_4In_2S_{8,}$ with H_2 production rates of 2.93, 2.86, 2.32, 2.15, and 2.05 mmol $h^{-1}g^{-1}$, respectively. Overall, it can be concluded that ternary metal chalcogenides with the formula $Zn_xIn_2S_{3+x}$ (x = 1–5) exhibit appropriate properties for use as photocatalysts, especially for water-splitting applications. In a different study, Fan et al. fabricated CuS@$ZnIn_2S_4$ hierarchical nanocages for H_2 evolution under visible light [89]. The presence of an interface between CuS and $ZnIn_2S_4$ improved the solar energy utilization and separation and transfer efficiency of photogenerated carriers. The as-prepared materials exhibited a photocatalytic H_2 evolution rate as high as 7910 μmol $h^{-1}g^{-1}$.

Table 2. Photocatalytic H_2 production activities using different ternary chalcogenides.

Photocatalyst Used	Amount of Photocatalyst Used	Electrolyte/ Solvent Used	Morphology	H_2 Produced	Ref.
MoS_2/g-C_3N_4/$ZnIn_2S_4$	50 mg	90 mL water and 10 mL triethanolamine	3D flower-like nanospheres	$ZnIn_2S_4$: 904 μmol $g^{-1}h^{-1}$ MoS_2/g-C_3N_4/$ZnIn_2S_4$ loaded with with 3 wt% g-C_3N_4 and 1.5 wt% MoS_2: 6291 μmol $g^{-1}h^{-1}$	[90]
$ZnIn_2S_4$@ $CuInS_2$	50 mg	0.25 mol/L Na_2S and 0.35 mol/L Na_2SO_3 as a sacrificial agent in 100 mL of aqueous solution	Marigold-like spherical structure comprising numerous thin nanosheets	1168 μmol g^{-1}	[91]
Ti_3C_2 MXene@ TiO_2/$CuInS_2$	10 mg	100 mL water solution containing 20% methanol as sacrificial agent	Layered structure decorated with small $CuInS_2$ nanoparticles	356.27 μmol $g^{-1}h^{-1}$	[92]
$ZnIn_2S_4$-rGO-$CuInS_2$	15 mg	50 mL of aqueous Na_2S/Na_2SO_3 (10 vol%) solution	Dispersed marigold-like structured $ZnIn_2S_4$ and layer-structured $CuInS_2$ on reduced graphene oxide sheets	2531 μmol/g after 5 h	[93]
CdS/$CoMoS_4$	80 mg	8 mL of lactic acid was added into 80 mL of water	Nanorod structured	7.5 at.% CdS/ $CoMoS_4$: 208 μmol h^{-1}	[94]
Carbon nanotube modified $Zn_{0.83}Cd_{0.17}S$	1 mg	40 mL of an aqueous solution containing 0.1 M Na_2S/0.02 M Na_2SO_3	Irregular	0.25 wt% carbon nanotube modified $Zn_{0.83}Cd_{0.17}S$: 5.41 mmol $h^{-1}g^{-1}$	[95]

In another report by Hojamberdiev and co-workers, they have synthesized layered crystals of trigonal $ZnIn_2S_4$ by a flux method using a range of binary fluxes, including $CaCl_2$:$InCl_3$, $SrCl_2$:$InCl_3$, $BaCl_2$:$InCl_3$, NaCl:$InCl_3$, KCl:$InCl_3$, and CsCl:$InCl_3$, from waste containing ZnS from the mining industry [7]. Among them, KCl:$InCl_3$ was the most favorable for synthesizing phase-pure trigonal $ZnIn_2S_4$. The trigonal $ZnIn_2S_4$ crystals grown in this study using KCl:$InCl_3$ flux exhibited higher photocatalytic H_2 evolution activity (132 μmol h^{-1}) in comparison to previously reported hexagonal $ZnIn_2S_4$ crystals prepared using the hydrothermal method. The superior performance obtained using the binary flux method can be ascribed to higher crystallinity and decreased defect density. The existence of secondary phases (namely ZnS and In_2S_3) in $ZnIn_2S_4$ crystals grown with $CaCl_2$:$InCl_3$ and NaCl:$InCl_3$ fluxes were found to have a positive impact on the photocatalytic activity, leading to H_2 evolution rates of 232 and 188 μmol h^{-1}, respectively. The enhanced H_2 production activity may be ascribed to efficient charge separation and interfacial charge transfer. Moreover, $Mn_{0.5}Cd_{0.5}S$/carbon black/CuS have been fabricated for H_2 production using sonochemical loading, and the subsequent in-situ deposition routes [96]. Lv et al. reported that the optimized $Mn_{0.5}Cd_{0.5}S$/carbon black/CuS exhibited the highest H_2 production of 819.9 μmol h^{-1}, which is 4.79-, 2.08-, and 1.47-fold increments more than pristine $Mn_{0.5}Cd_{0.5}S$, $Mn_{0.5}Cd_{0.5}S$/0.5 carbon black and $Mn_{0.5}Cd_{0.5}S$/CuS, respectively.

Group-III chalcogenide monolayers adopting two-faced 'Janus' structures are reported to be efficient photocatalysts for solar-driven water splitting. Several research groups have theoretically investigated the geometric structure, chemical stability, and electronic and optical properties of Janus group-III chalcogenide monolayers with layered ternary (XMMX′, where X, X′ = S, Se, or Te and M = Ga or In) [97,98] or quaternary composition (XMM′X′, where M and M′ are Ga and In) [99,100]. Among the ternary Janus monolayers, SGa_2Te, $SeGa_2Te$, SIn_2Te, and $SeIn_2Te$ are found to possess direct band gaps. Since direct gap semiconductors generally possess higher absorption coefficients than indirect gap semiconductors, these ternary group-III chalcogenide monolayers can potentially exhibit good light harvesting and efficient electron-hole pair generation [97]. However, most of these materials have not yet been synthesized, which will be an important next step in their photocatalytic evaluation. As reported by Bai and co-workers, group-III chalcogenide monolayers adopt a honeycomb-like geometric structure with a double M m (M = Ga or In) layer sandwiched between two chalcogen layers.

Depending on the combination of metal and chalcogen, both direct and indirect band gaps occur, with gap energies ranging from 1.54 eV to 2.91 eV. Although all these band gaps surpass the free energy change of the water-splitting reaction (1.23 eV per electron), photocatalytic water splitting is not guaranteed because the band edges must also straddle the water redox potentials. Figure 10 shows the calculated alignment between the band edges of the Janus XMMX′ monolayers and the water redox potentials. According to these calculations, all of the monolayers are capable of complete water splitting with the exception of SGa_2Te, which cannot drive the oxygen evolution reaction due to its valence band edge laying above the O_2/H_2O redox potential [97].

Although the pristine GaTe and InTe monolayers exhibit strong absorption at short wavelengths, they are inferior to the corresponding Janus monolayers at longer wavelengths. Among the Ga-based Janus chalcogenide monolayers, $SeGa_2Te$ and SGa_2Te possess the strongest optical absorption, while $SeIn_2Te$ and SIn_2Te exhibit the strongest absorption of all the Janus-type monolayers studied.

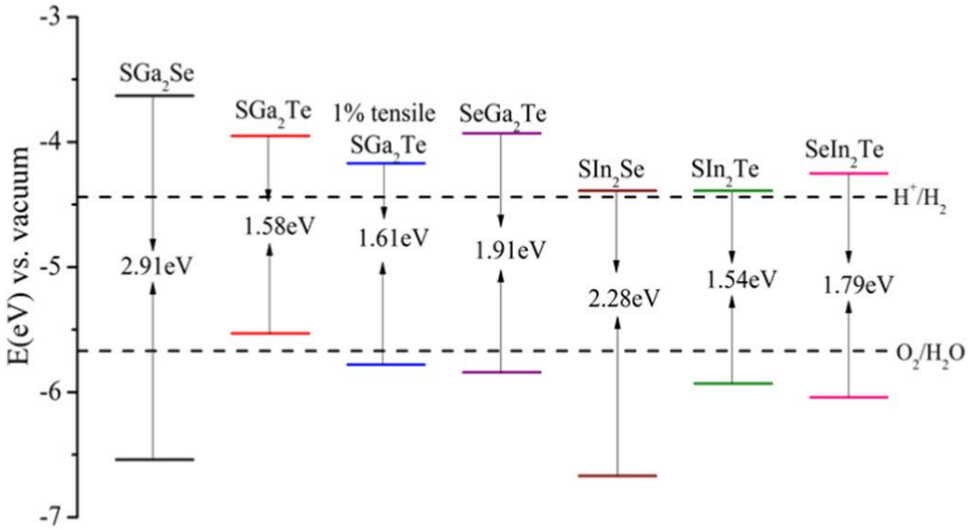

Figure 10. Calculated alignment of the band edges of the Janus XMMX′ monolayer with respect to the redox potentials of the water.

5. Prospects of Chalcogenides and Chalcogenide-Based Heterostructures

Even though steady progress has been made in utilizing chalcogenides as photocatalysts, a range of challenges still need to be addressed to promote the field, gain interest from other researchers, and achieve commercially exploitable results:

- In order to further boost the activity and stability of chalcogenides for water splitting, it is important to create precise methods for obtaining pure phase, active interface, exposed active surface, optimized electronic structure, and enhanced electronic conductivity.
- Recent research has shown that chalcogenides are very promising materials for H_2 evolution by photocatalytic water splitting. It is expected that, with further knowledge, controlled doping, surface engineering, and development of their performance can be further improved [101].
- Binary metal chalcogenides such as CdS and CdSe are unstable in acidic media and are also susceptible to photocorrosion. As such, potential replacements that are more stable in acidic media and that do not exhibit photocorrosion should be explored.
- Despite many recent studies on the use of ternary and quaternary chalcogenides as photocatalysts for H_2 production, the exact cause of photocorrosion in these materials is yet to be explored in detail and should be researched thoroughly in order to synthesize highly stable, multifunctional chalcogenides.
- Preparation of chalcogenide using low-cost methods while can produce large quantities of products also require more attention. Optimization of different parameters in the synthetic reactions such as precursors, temperature, pH, and reaction time should be studied for optimal yield to facilitate the production of these materials at a commercial scale.
- Detailed studies on extending the lifetime of photo-generated carriers and suppressing recombination are required to improve the photocatalytic activity of these materials for broader applications. Several approaches that could be employed include coupling with other semiconductors, loading of noble metals, and doping with metal or non-metal ions.

6. Conclusions

In summary, this review provides an overview of chalcogenide and chalcogenide-based heterostructures that have been extensively used for photocatalytic H_2O-splitting activities. This article summarizes the different modifications of chalcogenide materials that can improve their absorption of visible light ability, enhancing charge separation and reducing the recombination rate for water splitting. Moreover, this review also includes the mechanisms involved in the water splitting of binary, ternary, and chalcogenide-based heterostructures. Furthermore, combining different metal-based chalcogenides with other semiconductors has the potential to improve photocatalytic efficiency for generating H_2 and O_2 by water splitting.

Author Contributions: M.M.K.: Supervision, Conceptualization, Funding acquisition, Writing—review and editing. A.R.: Methodology, Data curation, Writing—original draft. All authors have read and agreed to the published version of the manuscript.

Funding: This research was funded by Universiti Brunei Darussalam, grant number UBD/RSCH/1.4/FICBF(b)/2021/035.

Acknowledgments: The authors would like to acknowledge the FIC block grant UBD/RSCH/1.4/FICBF(b)/2021/035 received from Universiti Brunei Darussalam, Brunei Darussalam.

Conflicts of Interest: The authors declare no conflict of interest.

References

1. Khan, M.M.; Ansari, S.A.; Pradhan, D.; Ansari, M.O.; Han, D.H.; Lee, J.; Cho, M.H. Band gap engineered TiO_2 nanoparticles for visible light induced photoelectrochemical and photocatalytic studies. *J. Mater. Chem. A* **2013**, *2*, 637–644. [CrossRef]
2. Rahman, A.; Harunsani, M.H.; Tan, A.L.; Khan, M.M. Zinc oxide and zinc oxide-based nanostructures: Biogenic and phytogenic synthesis, properties and applications. *Bioprocess Biosyst. Eng.* **2021**, *44*, 1333–1372. [CrossRef]
3. Matussin, S.; Harunsani, M.H.; Tan, A.L.; Khan, M.M. Plant-Extract-Mediated SnO_2 Nanoparticles: Synthesis and Applications. *ACS Sustain. Chem. Eng.* **2020**, *8*, 3040–3054. [CrossRef]
4. Khan, M.M.; Adil, S.F.; Al-Mayouf, A. Metal oxides as photocatalysts. *J. Saudi Chem. Soc.* **2015**, *19*, 462–464. [CrossRef]
5. Khan, M.M.; Rahman, A.; Matussin, S.N. Recent Progress of Metal-Organic Frameworks and Metal-Organic Frameworks-Based Heterostructures as Photocatalysts. *Nanomaterials* **2022**, *12*, 2820. [CrossRef]
6. Khan, M.M.; Pradhan, D.; Sohn, Y. *Nanocomposites for Visible Light-Induced Photocatalysis*; Springer: Berlin/Heidelberg, Germany, 2017. [CrossRef]
7. Hojamberdiev, M.; Cai, Y.; Vequizo, J.J.M.; Khan, M.M.; Vargas, R.; Yubuta, K.; Yamakata, A.; Teshima, K.; Hasegawa, M. Binary flux-promoted formation of trigonal $ZnIn_2S_4$ layered crystals using ZnS-containing industrial waste and their photocatalytic performance for H_2 production. *Green Chem.* **2018**, *20*, 3845–3856. [CrossRef]
8. Matussin, S.N.; Rahman, A.; Khan, M.M. Role of Anions in the Synthesis and Crystal Growth of Selected Semiconductors. *Front. Chem.* **2022**, *10*, 881518. [CrossRef]
9. Bouroushian, M. Chalcogens and Metal Chalcogenides. In *Electrochemistry of Metal Chalcogenides*; Monographs in Electrochemistry; Springer: Berlin/Heidelberg, Germany, 2010; pp. 1–56. [CrossRef]
10. Rahman, A.; Khan, M.M. Chalcogenides as photocatalysts. *New J. Chem.* **2021**, *45*, 19622–19635. [CrossRef]
11. Choi, Y.I.; Lee, S.; Kim, S.K.; Kim, Y.-I.; Cho, D.W.; Khan, M.M.; Sohn, Y. Fabrication of ZnO, ZnS, Ag-ZnS, and Au-ZnS microspheres for photocatalytic activities, CO oxidation and 2-hydroxyterephthalic acid synthesis. *J. Alloys Compd.* **2016**, *675*, 46–56. [CrossRef]
12. Khan, M.E.; Cho, M.H. CdS-graphene Nanocomposite for Efficient Visible-light-driven Photocatalytic and Photoelectrochemical Applications. *J. Colloid Interface Sci.* **2016**, *482*, 221–232. [CrossRef]
13. Khan, M.M. *Chalcogenide-Based Nanomaterials as Photocatalysts*; Elsevier: Amsterdam, The Netherlands, 2021. [CrossRef]
14. Tian, M.-W.; Yuen, H.-C.; Yan, S.-R.; Huang, W.-L. The multiple selections of fostering applications of hydrogen energy by integrating economic and industrial evaluation of different regions. *Int. J. Hydrogen Energy* **2019**, *44*, 29390–29398. [CrossRef]
15. Chen, Y.; Feng, X.; Liu, M.; Su, J.; Shen, S. Towards efficient solar-to-hydrogen conversion: Fundamentals and recent progress in copper-based chalcogenide photocathodes. *Nanophotonics* **2016**, *5*, 524–547. [CrossRef]
16. Revankar, S.T. Nuclear hydrogen production. In *Storage and Hybridization of Nuclear Energy: Techno-Economic Integration of Renewable and Nuclear Energy*; Elsevier: Amsterdam, The Netherlands, 2018; pp. 49–117. [CrossRef]
17. Yerga, R.M.N.; Alvarez-Galvan, M.C.; Del Valle, F.; De La Mano, J.A.V.; Fierro, J.L.G. Water Splitting on Semiconductor Catalysts under Visible-Light Irradiation. *ChemSusChem* **2009**, *2*, 471–485. [CrossRef] [PubMed]
18. Maeda, K.; Domen, K. New Non-Oxide Photocatalysts Designed for Overall Water Splitting under Visible Light. *J. Phys. Chem. C* **2007**, *111*, 7851–7861. [CrossRef]

19. Maeda, K.; Lu, D.; Domen, K. Direct Water Splitting into Hydrogen and Oxygen under Visible Light by using Modified TaON Photocatalysts with d^0Electronic Configuration. *Chem. A Eur. J.* **2013**, *19*, 4986–4991. [CrossRef] [PubMed]
20. Walter, M.G.; Warren, E.L.; McKone, J.R.; Boettcher, S.W.; Mi, Q.; Santori, E.A.; Lewis, N.S. Solar Water Splitting Cells. *Chem. Rev.* **2010**, *110*, 6446–6473. [CrossRef]
21. Li, X.; Zuo, X.; Jiang, X.; Li, D.; Cui, B.; Liu, D. Enhanced photocatalysis for water splitting in layered tin chalcogenides with high carrier mobility. *Phys. Chem. Chem. Phys.* **2019**, *21*, 7559–7566. [CrossRef]
22. Kannan, S.; Vinitha, P.; Mohanraj, K.; Sivakumar, G. Antibacterial studies of novel Cu2WS4 ternary chalcogenide synthesized by hydrothermal process. *J. Solid State Chem.* **2018**, *258*, 376–382. [CrossRef]
23. Sarilmaz, A.; Can, M.; Ozel, F. Ternary copper tungsten selenide nanosheets synthesized by a facile hot-injection method. *J. Alloys Compd.* **2017**, *699*, 479–483. [CrossRef]
24. Saravanan, K.; Selladurai, S.; Ananthakumar, S.; Suriakarthick, R. Solvothermal synthesis of copper cadmium sulphide ($CuCdS_2$) nanoparticles and its structural, optical and morphological properties. *Mater. Sci. Semicond. Process.* **2019**, *93*, 345–356. [CrossRef]
25. Khalil, A.A.I.; El-Gawad, A.-S.H.A.; Gadallah, A.-S. Impact of silver dopants on structural, morphological, optical, and electrical properties of copper-zinc sulfide thin films prepared via sol-gel spin coating method. *Opt. Mater.* **2020**, *109*, 110250. [CrossRef]
26. Gu, X.; Tan, C.; He, L.; Guo, J.; Zhao, X.; Qi, K.; Yan, Y. Mn^{2+} doped $AgInS_2$ photocatalyst for formaldehyde degradation and hydrogen production from water splitting by carbon tube enhancement. *Chemosphere* **2022**, *304*, 135292. [CrossRef]
27. Wang, X.; Feng, Z.; Fan, D.; Fan, F.; Li, C. Shape-Controlled Synthesis of CdS Nanostructures via a Solvothermal Method. *Cryst. Growth Des.* **2010**, *10*, 5312–5318. [CrossRef]
28. Hu, Z.; Chen, T.; Xie, Z.; Guo, C.; Jiang, W.; Chen, Y.; Xu, Y. Emission tunable $AgInS_2$ quantum dots synthesized via microwave method for white light-emitting diodes application. *Opt. Mater.* **2022**, *124*, 111975. [CrossRef]
29. Li, S.; Cai, M.; Liu, Y.; Wang, C.; Yan, R.; Chen, X. Constructing $Cd_{0.5}Zn_{0.5}S/Bi_2WO_6$ S-scheme heterojunction for boosted photocatalytic antibiotic oxidation and Cr(VI) reduction. *Adv. Powder Mater.* **2023**, *2*, 100073. [CrossRef]
30. Thompson, M.J.; Ruberu, T.P.A.; Blakeney, K.J.; Torres, K.V.; Dilsaver, P.S.; Vela, J. Axial Composition Gradients and Phase Segregation Regulate the Aspect Ratio of Cu_2ZnSnS_4 Nanorods. *J. Phys. Chem. Lett.* **2013**, *4*, 3918–3923. [CrossRef]
31. Mandari, K.K.; Son, N.; Kang, M. CuS/Ag_2O nanoparticles on ultrathin g-C_3N_4 nanosheets to achieve high performance solar hydrogen evolution. *J. Colloid Interface Sci.* **2022**, *615*, 740–751. [CrossRef]
32. Yin, M.; Sun, J.; Li, Y.; Ye, Y.; Liang, K.; Fan, Y.; Li, Z. Efficient photocatalytic hydrogen evolution over MoS_2/activated carbon composite sensitized by Erythrosin B under LED light irradiation. *Catal. Commun.* **2020**, *142*, 106029. [CrossRef]
33. Yang, Z.; Xie, X.; Zhang, Z.; Yang, J.; Yu, C.; Dong, S.; Xiang, M.; Qin, H. NiS_2@V_2O_5/VS_2 ternary heterojunction for a high-performance electrocatalyst in overall water splitting. *Int. J. Hydrogen Energy* **2022**, *47*, 27338–27346. [CrossRef]
34. Gopalakrishnan, S.; Paulraj, G.; Eswaran, M.K.; Ray, A.; Singh, N.; Jeganathan, K. VS_2 wrapped Si nanowires as core-shell heterostructure photocathode for highly efficient photoelectrochemical water reduction performance. *Chemosphere* **2022**, *302*, 134708. [CrossRef]
35. Tang, Y.; Li, X.; Zhang, D.; Pu, X.; Ge, B.; Huang, Y. Noble metal-free ternary $MoS_2/Zn_{0.5}Cd_{0.5}S$/g-C_3N_4 heterojunction composite for highly efficient photocatalytic H_2 production. *Mater. Res. Bull.* **2018**, *110*, 214–222. [CrossRef]
36. Arai, T.; Senda, S.-I.; Sato, Y.; Takahashi, H.; Shinoda, K.; Jeyadevan, B.; Tohji, K. Cu-Doped ZnS Hollow Particle with High Activity for Hydrogen Generation from Alkaline Sulfide Solution under Visible Light. *Chem. Mater.* **2008**, *20*, 1997–2000. [CrossRef]
37. Oliva, A. Formation of the band gap energy on CdS thin films growth by two different techniques. *Thin Solid Films* **2001**, *391*, 28–35. [CrossRef]
38. Cheng, L.; Xiang, Q.; Liao, Y.; Zhang, H. CdS-Based photocatalysts. *Energy Environ. Sci.* **2018**, *11*, 1362–1391. [CrossRef]
39. Li, C.; Yuan, J.; Han, B.; Shangguan, W. Synthesis and photochemical performance of morphology-controlled CdS photocatalysts for hydrogen evolution under visible light. *Int. J. Hydrogen Energy* **2011**, *36*, 4271–4279. [CrossRef]
40. Garg, P.; Bhauriyal, P.; Mahata, A.; Rawat, K.S.; Pathak, B. Role of Dimensionality for Photocatalytic Water Splitting: CdS Nanotube versus Bulk Structure. *ChemPhysChem* **2018**, *20*, 383–391. [CrossRef]
41. Luo, M.; Liu, Y.; Hu, J.; Liu, H.; Li, J. One-Pot Synthesis of CdS and Ni-Doped CdS Hollow Spheres with Enhanced Photocatalytic Activity and Durability. *ACS Appl. Mater. Interfaces* **2012**, *4*, 1813–1821. [CrossRef]
42. Zhen, W.; Ning, X.; Yang, B.; Wu, Y.; Li, Z.; Lu, G. The enhancement of CdS photocatalytic activity for water splitting via anti-photocorrosion by coating Ni2P shell and removing nascent formed oxygen with artificial gill. *Appl. Catal. B Environ.* **2018**, *221*, 243–257. [CrossRef]
43. Li, Y.-H.; Qi, M.-Y.; Li, J.-Y.; Tang, Z.-R.; Xu, Y.-J. Noble metal free CdS@CuS-NixP hybrid with modulated charge transfer for enhanced photocatalytic performance. *Appl. Catal. B Environ.* **2019**, *257*, 117934. [CrossRef]
44. Yang, J.; Yan, H.; Wang, X.; Wen, F.; Wang, Z.; Fan, D.; Shi, J.; Li, C. Roles of cocatalysts in Pt–PdS/CdS with exceptionally high quantum efficiency for photocatalytic hydrogen production. *J. Catal.* **2012**, *290*, 151–157. [CrossRef]
45. Yang, T.-T.; Chen, W.-T.; Hsu, Y.-J.; Wei, K.-H.; Lin, T.-Y. Interfacial Charge Carrier Dynamics in Core−Shell Au-CdS Nanocrystals. *J. Phys. Chem. C* **2010**, *114*, 11414–11420. [CrossRef]
46. Tso, S.; Li, W.-S.; Wu, B.-H.; Chen, L.-J. Enhanced H_2 production in water splitting with CdS-ZnO core-shell nanowires. *Nano Energy* **2017**, *43*, 270–277. [CrossRef]
47. Zhang, F.; Zhuang, H.-Q.; Zhang, W.; Yin, J.; Cao, F.-H.; Pan, Y.-X. Noble-metal-free CuS/CdS photocatalyst for efficient visible-light-driven photocatalytic H_2 production from water. *Catal. Today* **2018**, *330*, 203–208. [CrossRef]

48. Cheng, F.; Xiang, Q. A solid-state approach to fabricate a CdS/CuS nano-heterojunction with promoted visible-light photocatalytic H_2-evolution activity. *RSC Adv.* **2016**, *6*, 76269–76272. [CrossRef]
49. Wu, Z.; Zhao, G.; Zhang, Y.-N.; Tian, H.; Li, D. Enhanced Photocurrent Responses and Antiphotocorrosion Performance of CdS Hybrid Derived from Triple Heterojunction. *J. Phys. Chem. C* **2012**, *116*, 12829–12835. [CrossRef]
50. Holmes, M.A.; Townsend, T.K.; Osterloh, F.E. Quantum confinement controlled photocatalytic water splitting by suspended CdSe nanocrystals. *Chem. Commun.* **2011**, *48*, 371–373. [CrossRef]
51. Yang, Q.; Luo, M.; Liu, K.; Cao, H.; Yan, H. Covalent organic frameworks for photocatalytic applications. *Appl. Catal. B Environ.* **2020**, *276*, 119174. [CrossRef]
52. You, J.; Zhao, Y.; Wang, L.; Bao, W. Recent developments in the photocatalytic applications of covalent organic frameworks: A review. *J. Clean. Prod.* **2021**, *291*, 125822. [CrossRef]
53. You, D.; Pan, Z.; Cheng, Q. COFs-Ph@CdS S-scheme heterojunctions with photocatalytic hydrogen evolution and efficient degradation properties. *J. Alloys Compd.* **2023**, *930*, 167069. [CrossRef]
54. Das, A.; Han, Z.; Haghighi, M.G.; Eisenberg, R. Photogeneration of hydrogen from water using CdSe nanocrystals demonstrating the importance of surface exchange. *Proc. Natl. Acad. Sci. USA* **2013**, *110*, 16716–16723. [CrossRef]
55. Park, Y.; Park, B. Effect of ligand exchange on photocurrent enhancement in cadmium selenide (CdSe) quantum dot water splitting cells. *Results Phys.* **2018**, *11*, 162–165. [CrossRef]
56. Zhou, W.; Li, F.; Yang, X.; Yang, W.; Wang, C.; Cao, R.; Zhou, C.; Tian, M. Peanut-chocolate-ball-inspired construction of the interface engineering between CdS and intergrown Cd: Boosting both the photocatalytic activity and photocorrosion resistance. *J. Energy Chem.* **2023**, *76*, 75–89. [CrossRef]
57. Li, K.; Pan, H.; Wang, F.; Zhang, Z.; Min, S. In-situ exsolved NiS nanoparticle-socketed CdS with strongly coupled interfaces as a superior visible-light-driven photocatalyst for hydrogen evolution. *Appl. Catal. B Environ.* **2023**, *321*, 122028. [CrossRef]
58. Basu, M.; Nazir, R.; Fageria, P.; Pande, S. Construction of CuS/Au Heterostructure through a Simple Photoreduction Route for Enhanced Electrochemical Hydrogen Evolution and Photocatalysis. *Sci. Rep.* **2016**, *6*, 34738. [CrossRef]
59. Chandra, M.; Bhunia, K.; Pradhan, D. Controlled Synthesis of CuS/TiO_2 Heterostructured Nanocomposites for Enhanced Photocatalytic Hydrogen Generation through Water Splitting. *Inorg. Chem.* **2018**, *57*, 4524–4533. [CrossRef]
60. Dubale, A.A.; Tamirat, A.G.; Chen, H.-M.; Berhe, T.A.; Pan, C.-J.; Su, W.-N.; Hwang, B.-J. A highly stable CuS and CuS–Pt modified Cu_2O/CuO heterostructure as an efficient photocathode for the hydrogen evolution reaction. *J. Mater. Chem. A* **2015**, *4*, 2205–2216. [CrossRef]
61. Ma, L.; Yang, D.-J.; Song, X.-P.; Li, H.-X.; Ding, S.-J.; Xiong, L.; Qin, P.-L.; Chen, X.-B. Pt Decorated (Au Nanosphere)/(CuSe Ultrathin Nanoplate) Tangential Hybrids for Efficient Photocatalytic Hydrogen Generation via Dual-Plasmon-Induced Strong VIS–NIR Light Absorption and Interfacial Electric Field Coupling. *Sol. RRL* **2019**, *4*, 1900376. [CrossRef]
62. Liang, H.; Mei, J.; Sun, H.; Cao, L. Enhanced photocatalytic hydrogen evolution of CdS@CuS core-shell nanorods under visible light. *Mater. Sci. Semicond. Process.* **2023**, *153*, 107105. [CrossRef]
63. Hou, J.; Huang, B.; Kong, L.; Xie, Y.; Liu, Y.; Chen, M.; Wang, Q. One-pot hydrothermal synthesis of CdS–CuS decorated TiO_2 NTs for improved photocatalytic dye degradation and hydrogen production. *Ceram. Int.* **2021**, *47*, 30860–30868. [CrossRef]
64. Zhuang, H.L.; Hennig, R.G. Single-Layer Group-III Monochalcogenide Photocatalysts for Water Splitting. *Chem. Mater.* **2013**, *25*, 3232–3238. [CrossRef]
65. Peng, Q.; Xiong, R.; Sa, B.; Zhou, J.; Wen, C.; Wu, B.; Anpo, M.; Sun, Z. Computational mining of photocatalysts for water splitting hydrogen production: Two-dimensional InSe-family monolayers. *Catal. Sci. Technol.* **2017**, *7*, 2744–2752. [CrossRef]
66. Peng, Q.; Guo, Z.; Sa, B.; Zhou, J.; Sun, Z. New gallium chalcogenides/arsenene van der Waals heterostructures promising for photocatalytic water splitting. *Int. J. Hydrogen Energy* **2018**, *43*, 15995–16004. [CrossRef]
67. Gupta, U.; Rao, C. Hydrogen generation by water splitting using MoS_2 and other transition metal dichalcogenides. *Nano Energy* **2017**, *41*, 49–65. [CrossRef]
68. Rahman, A.; Jennings, J.R.; Tan, A.L.; Khan, M.M. Molybdenum Disulfide-Based Nanomaterials for Visible-Light-Induced Photocatalysis. *ACS Omega* **2022**, *7*, 22089–22110. [CrossRef]
69. Li, M.; Cui, Z.; Li, E. Silver-modified MoS_2 nanosheets as a high-efficiency visible-light photocatalyst for water splitting. *Ceram. Int.* **2019**, *45*, 14449–14456. [CrossRef]
70. Yuan, Y.-J.; Chen, D.; Zhong, J.; Yang, L.-X.; Wang, J.; Liu, M.-J.; Tu, W.-G.; Yu, Z.-T.; Zou, Z.-G. Interface engineering of a noble-metal-free 2D–2D MoS_2/Cu-$ZnIn_2S_4$ photocatalyst for enhanced photocatalytic H_2 production. *J. Mater. Chem. A* **2017**, *5*, 15771–15779. [CrossRef]
71. Hassan, M.A.; Kim, M.-W.; Johar, M.A.; Waseem, A.; Kwon, M.-K.; Ryu, S.-W. Transferred monolayer MoS_2 onto GaN for heterostructure photoanode: Toward stable and efficient photoelectrochemical water splitting. *Sci. Rep.* **2019**, *9*, 20141. [CrossRef]
72. Zhao, G.; Wang, X.; Wang, S.; Rui, K.; Chen, Y.; Yu, H.; Ma, J.; Dou, S.X.; Sun, W. Heteroatom-doped MoSe $_2$ Nanosheets with Enhanced Hydrogen Evolution Kinetics for Alkaline Water Splitting. *Chem. Asian J.* **2018**, *14*, 301–306. [CrossRef]
73. Lei, W.; Wang, F.; Pan, X.; Ye, Z.; Lu, B. Z-scheme MoO_3-2D SnS nanosheets heterojunction assisted g-C_3N_4 composite for enhanced photocatalytic hydrogen evolutions. *Int. J. HydrogEN Energy* **2022**, *47*, 10877–10890. [CrossRef]
74. Liu, Y.; Zhou, Y.; Zhou, X.; Jin, X.; Li, B.; Liu, J.; Chen, G. Cu doped SnS_2 nanostructure induced sulfur vacancy towards boosted photocatalytic hydrogen evolution. *Chem. Eng. J.* **2020**, *407*, 127180. [CrossRef]

75. Geng, Y.; Zou, X.; Lu, Y.; Wang, L. Fabrication of the $SnS_2/ZnIn_2S_4$ heterojunction for highly efficient visible light photocatalytic H_2 evolution. *Int. J. Hydrogen Energy* **2022**, *47*, 11520–11527. [CrossRef]
76. Li, Y.-Y.; Wang, J.-G.; Sun, H.-H.; Hua, W.; Liu, X.-R. Heterostructured SnS_2/SnO_2 nanotubes with enhanced charge separation and excellent photocatalytic hydrogen production. *Int. J. Hydrogen Energy* **2018**, *43*, 14121–14129. [CrossRef]
77. Mangiri, R.; Kumar, K.S.; Subramanyam, K.; Ratnakaram, Y.; Sudharani, A.; Reddy, D.A.; Vijayalakshmi, R. Boosting solar driven hydrogen evolution rate of CdS nanorods adorned with MoS_2 and SnS_2 nanostructures. *Colloids Interface Sci. Commun.* **2021**, *43*, 100437. [CrossRef]
78. Barawi, M.; Flores, E.; Ferrer, I.J.; Ares, J.R.; Sánchez, C. Titanium trisulphide (TiS_3) nanoribbons for easy hydrogen photogeneration under visible light. *J. Mater. Chem. A* **2015**, *3*, 7959–7965. [CrossRef]
79. Flores, E.; Ares, J.; Sánchez, C.; Ferrer, I. Ternary transition titanium-niobium trisulfide as photoanode for assisted water splitting. *Catal. Today* **2018**, *321–322*, 107–112. [CrossRef]
80. Guo, W.; Wu, D. Facile synthesis of VS4/graphene nanocomposites and their visible-light-driven photocatalytic water splitting activities. *Int. J. Hydrogen Energy* **2014**, *39*, 16832–16840. [CrossRef]
81. Ikeda, S.; Aono, N.; Iwase, A.; Kobayashi, H.; Kudo, A. Cu_3MS_4 (M=V, Nb, Ta) and its Solid Solutions with Sulvanite Structure for Photocatalytic and Photoelectrochemical H_2 Evolution under Visible-Light Irradiation. *ChemSusChem* **2018**, *12*, 1977–1983. [CrossRef]
82. Li, G.; Deng, X.; Chen, P.; Wang, X.; Ma, J.; Liu, F.; Yin, S.-F. Sulphur vacancies-VS_2@C_3N_4 drived by in situ supramolecular self-assembly for synergistic photocatalytic degradation of real wastewater and H_2 production: Vacancies taming interfacial compact heterojunction and carriers transfer. *Chem. Eng. J.* **2022**, *433*, 134505. [CrossRef]
83. Zhong, X.; Tang, J.; Wang, J.; Shao, M.; Chai, J.; Wang, S.; Yang, M.; Yang, Y.; Wang, N.; Wang, S.; et al. 3D heterostructured pure and N-Doped Ni_3S_2/VS_2 nanosheets for high efficient overall water splitting. *Electrochim. Acta* **2018**, *269*, 55–61. [CrossRef]
84. Kurnia, F.; Ng, Y.H.; Amal, R.; Valanoor, N.; Hart, J.N. Defect engineering of ZnS thin films for photoelectrochemical water-splitting under visible light. *Sol. Energy Mater. Sol. Cells* **2016**, *153*, 179–185. [CrossRef]
85. Sánchez-Tovar, R.; Fernández-Domene, R.M.; Montañés, M.T.; Sanz-Marco, A.; Garcia-Antón, J. ZnO/ZnS heterostructures for hydrogen production by photoelectrochemical water splitting. *RSC Adv.* **2016**, *6*, 30425–30435. [CrossRef]
86. Zhang, X.; Zhou, Y.-Z.; Wu, D.-Y.; Liu, X.-H.; Zhang, R.; Liu, H.; Dong, C.-K.; Yang, J.; Kulinich, S.A.; Du, X.-W. ZnO nanosheets with atomically thin ZnS overlayers for photocatalytic water splitting. *J. Mater. Chem. A* **2018**, *6*, 9057–9063. [CrossRef]
87. Lee, G.-J.; Anandan, S.; Masten, S.J.; Wu, J.J. Photocatalytic hydrogen evolution from water splitting using Cu doped ZnS microspheres under visible light irradiation. *Renew. Energy* **2016**, *89*, 18–26. [CrossRef]
88. Wu, Y.; Wang, H.; Tu, W.; Wu, S.; Chew, J.W. Effects of composition faults in ternary metal chalcogenides (Zn In_2S_3+, x = 1 − 5) layered crystals for visible-light-driven catalytic hydrogen generation and carbon dioxide reduction. *Appl. Catal. B Environ.* **2019**, *256*, 117810. [CrossRef]
89. Fan, H.-T.; Wu, Z.; Liu, K.-C.; Liu, W.-S. Fabrication of 3D CuS@$ZnIn_2S_4$ hierarchical nanocages with 2D/2D nanosheet subunits p-n heterojunctions for improved photocatalytic hydrogen evolution. *Chem. Eng. J.* **2022**, *433*, 134474. [CrossRef]
90. Ni, T.; Yang, Z.; Cao, Y.; Lv, H.; Liu, Y. Rational design of MoS_2/g-$C_3N_4/ZnIn_2S_4$ hierarchical heterostructures with efficient charge transfer for significantly enhanced photocatalytic H_2 production. *Ceram. Int.* **2021**, *47*, 22985–22993. [CrossRef]
91. Guo, X.; Peng, Y.; Liu, G.; Xie, G.; Guo, Y.; Zhang, Y.; Yu, J. An Efficient $ZnIn_2S_4$@$CuInS_2$ Core–Shell p–n Heterojunction to Boost Visible-Light Photocatalytic Hydrogen Evolution. *J. Phys. Chem. C* **2020**, *124*, 5934–5943. [CrossRef]
92. Yang, W.; Ma, G.; Fu, Y.; Peng, K.; Yang, H.; Zhan, X.; Yang, W.; Wang, L.; Hou, H. Rationally designed Ti_3C_2 MXene@$TiO_2/CuInS_2$ Schottky/S-scheme integrated heterojunction for enhanced photocatalytic hydrogen evolution. *Chem. Eng. J.* **2021**, *429*, 132381. [CrossRef]
93. Raja, A.; Son, N.; Swaminathan, M.; Kang, M. Facile synthesis of sphere-like structured $ZnIn_2S_4$-rGO-$CuInS_2$ ternary heterojunction catalyst for efficient visible-active photocatalytic hydrogen evolution. *J. Colloid Interface Sci.* **2021**, *602*, 669–679. [CrossRef]
94. Li, Q.; Qiao, X.-Q.; Jia, Y.; Hou, D.; Li, D.-S. Amorphous $CoMoS_4$ Nanostructure for Photocatalytic H_2 Generation, Nitrophenol Reduction, and Methylene Blue Adsorption. *ACS Appl. Nano Mater.* **2019**, *3*, 68–76. [CrossRef]
95. Yao, Z.; Wang, L.; Zhang, Y.; Yu, Z.; Jiang, Z. Carbon nanotube modified $Zn_{0.83}Cd_{0.17}S$ nanocomposite photocatalyst and its hydrogen production under visible-light. *Int. J. Hydrogen Energy* **2014**, *39*, 15380–15386. [CrossRef]
96. Lv, H.; Kong, Y.; Gong, Z.; Zheng, J.; Liu, Y.; Wang, G. Engineering multifunctional carbon black interface over $Mn_{0.5}Cd_{0.5}S$ nanoparticles/CuS nanotubes heterojunction for boosting photocatalytic hydrogen generation activity. *Appl. Surf. Sci.* **2022**, *604*, 154513. [CrossRef]
97. Bai, Y.; Zhang, Q.; Xu, N.; Deng, K.; Kan, E. The Janus structures of group-III chalcogenide monolayers as promising photocatalysts for water splitting. *Appl. Surf. Sci.* **2019**, *478*, 522–531. [CrossRef]
98. Hu, L.; Wei, D. Janus Group-III Chalcogenide Monolayers and Derivative Type-II Heterojunctions as Water-Splitting Photocatalysts with Strong Visible-Light Absorbance. *J. Phys. Chem. C* **2018**, *122*, 27795–27802. [CrossRef]
99. Wang, P.; Zong, Y.; Liu, H.; Wen, H.; Wu, H.-B.; Xia, J.-B. Highly efficient photocatalytic water splitting and enhanced piezoelectric properties of 2D Janus group-III chalcogenides. *J. Mater. Chem. C* **2021**, *9*, 4989–4999. [CrossRef]

100. Ahmad, I.; Shahid, I.; Ali, A.; Gao, L.; Cai, J. Electronic, mechanical, optical and photocatalytic properties of two-dimensional Janus XGaInY (X, Y;= S, Se and Te) monolayers. *RSC Adv.* **2021**, *11*, 17230–17239. [CrossRef]
101. Chu, S.; Li, W.; Yan, Y.; Hamann, T.; Shih, I.; Wang, D.; Mi, Z. Roadmap on solar water splitting: Current status and future prospects. *Nano Futur.* **2017**, *1*, 022001. [CrossRef]